Effect of angle in removing proteins or bacteria on a tilted surface using air bubbles

Alireza Hooshanginejad [1,2] Timothy Sheppard,[1] Purui Xu,[3] Janeth Manyalla,[1] John Jaicks [1]
Ehsan Esmaili,[4] and Sunghwan Jung [1,*]

[1]*Department of Biological and Environmental Engineering, Cornell University,
Ithaca, New York 14850, USA*
[2]*School of Engineering, Brown University, Providence, Rhode Island 02912, USA*
[3]*Department of Biomedical Engineering, Cornell University, Ithaca, New York 14850, USA*
[4]*Department of Mechanical Engineering, Purdue University, West Lafayette, Indiana 47907, USA*

Cleaning surfaces with air bubbles in an aqueous medium has been a topic of discussion in recent years due to the growing interest in sustainable methods for cleaning biological surfaces such as agricultural produce. Specifically, in a bubble-injection method, inclined surfaces are targeted by many millimetric air bubbles that collide with and slide along the surface. The collision and subsequent sliding of these air bubbles exert shear stress on the surface, causing contaminants to be removed. The shear stress is proportional to the tangential speed of the bubble with respect to the surface divided by the thickness of the thin film of liquid between the bubble and the solid surface. In this study, we conduct experiments to test the cleaning efficacy at different angles of inclination of a contaminated surface. We use two different types of surface coated with either a protein solution or a bacterial biofilm. Our experimental results indicate that bubbles exhibit the highest cleaning efficacy at the surface angle of $\theta \approx 20º$ with respect to the horizontal plane for polydisperse bubbles in the range of 0.3–2 mm and with an average radius of 0.6 mm. To gain a better understanding of the underlying mechanism, we perform a numerical analysis of a single air bubble colliding with a clean surface at various angles. Our numerical and theoretical results show that the average shear force that the bubble exerts on the surface reaches a maximum at $\theta \approx 22.5º$ which agrees well with the experiments. We also compare the maximum shear stress in sliding phase with the shear stress required for removing different types of bacteria as a fluid-mechanics-based guideline for geometrical design of bubble cleaning devices.

I. INTRODUCTION

Multiphase flows have been used for the removal of micrometer-scale contaminants from surfaces for the past few decades [1–3]. Specifically, air bubbles are proposed as a sustainable cleaning method for wastewater treatments [4–6] or preventing biofouling [7,8]. Acoustic bubble cavitation [9,10] and nonacoustic collision and sliding of submillimetric bubbles [11] are the two common methods of contaminant removal with air bubbles. Despite the differences in how bubbles are originated in the two, both methods use the same principle, namely exerting shear stress over the surface. While extensive attention has been paid to studying cavitation bubbles in the context of cleaning [9,10,12–15], few studies exist on cleaning effect of sliding bubbles [7,11,16]. Recently,

---

*sunnyjsh@cornell.edu

agricultural produce such as fruits and vegetables have been cleaned with the insertion of air bubbles [10,11,17]. Developing such environmentally benign methods for sanitizing agricultural produce is important, as pathogens in fresh produce are recognized as the primary cause of foodborne diseases in millions of people each year [18–20].

Bubble dynamics has been studied extensively in both a freely rising bubble [21–25] and a bubble interacting with either horizontal [26–31] or vertical [32–35] solid surfaces. However, only a few studies have investigated the dynamics of bubbles along a tilted solid surface [36–45]. Specifically, by incorporating lubrication approximation the thin film flow between the sliding bubble and the surface can be modeled [11,39]. Then the shear stress can be quantified on the surface, which is the key to characterizing the cleaning effect of sliding bubbles. Although shear stress was recently calculated for varying surface angles [11], no experiments have yet verified the cleaning effect of air bubbles on tilted surfaces. In addition, while the maximum shear stress on the surface has been reported for different inclination angles [11], the average shear stress has not been studied for practical applications and comparison with potential experiments.

Bacteria sorption to surfaces is composed of two stages [46–49]. Bacteria are first attracted to the surface where it still shows Brownian motion near the surface [47]. This *reversible sorption* of bacteria is weak, and the bacteria can be removed with gentle forces or washing with low concentrations of NaCl [48]. Within a few hours of reversible sorption, biosynthesis formation of extracellular polymer substances results in the irreversible stage of bacteria sorption [46,48]. The irreversible sorption yields a firm adhesion to the surface, where the bacteria no longer exhibits Brownian motion [47,49]. From a practical point of view, shear force of different magnitude is required to remove biofilms of different type [50]. Such critical force depends on the physiochemical properties of the surface and the bacteria [51–53]. For instance, in a laminar flow, *Escherichia coli* (*E. coli*) can be removed with a shear stress of 0.03–5 N.m^{-2} [51], while the shear stress for removing *Listeria monocytogenes* from a stainless steel surface varies from 24 to 144 Pa [54]. presence of microbubbles in the channel increases the detachment rate of *Actinomyces naeslundii* bacteria from 40% to 98% [55]. Recently, numerical analysis of a bubble colliding with and sliding on a tilted surface has shown that the shear stress exerted on the surface is sufficient for removing biofilms of several bacteria strains from the surface [11].

In this study, we probe the effect of surface inclination angle on the shear stress exerted on the surface by sliding millimetric bubbles aimed for removing protein layers or *E. coli* biofilms from the surface. Our experimental results show that there exists a critical angle for maximum cleaning effect. In addition, we perform numerical calculations of an air bubble impacting and sliding over a clean tilted surface incorporating the recent model on bubble dynamics near a tilted wall [11]. The manuscript is organized as follows. In Sec. II, we discuss experimental methods including the coating procedure in Sec. II A and the cleaning experiments in Sec. II B, and numerical methods in Sec. II C. We then present and discuss our experimental and computational results in Sec. III. Finally, in Sec. IV we summarize our findings and discuss future studies.

II. MATERIALS AND METHODS

A. Coating preparation

1. Protein dirt preparation

A protein dirt/soil solution is synthesized for glass slide coating. We first incorporate 100 g of 2% fat milk and 30 g of sifted wheat flour in a small pot with an immersion blender until the mixture reaches 115°C, and a pastelike solid is formed. This mixture is then left to cool to 30°C, wherein afterwards it is combined with another 120 g of milk and is blended again until a uniform solution remains after 10 min. Next, 6 g of Nigrosin dye is gently stirred in with a wooden tongue depressor until fully combined. Once completed, the mixture is sifted twice, first through a 500–600 μm mesh, then again through a 100–150 μm mesh. The resulting mixture is then ready to be used for coating.

2. Spin coating of protein dirt

On the same day as protein preparation, glass microscope slides of 76.2 mm × 25.4 mm × 1.1 mm are cleaned and coated with the protein solution using a custom-designed spin coater. More information about making the spin coater, including three-dimensional (3D) printing designs, can be found in Ref. [45]. To coat the slides, we first secure the slide tightly to the spin-coater plate with opposing metal bolts. Next, a 0.5 ml protein drop is gently deposited onto the middle of the slide and spun for 10 s at a rate of $\Omega \sim 1100$–1200 rotations per minute (RPM). These coated slides are left to dry for 15 min inside a fume hood, then proceeded by a second coating of the same procedure. This second coating creates a more opaque surface which proved to be more effective in characterizing the cleaning effect of our tests. After the second coating, the slides are stored in a cool, dry place. In the current study, all slides are tested after drying for two full days. We note that the effect of the drying time was investigated in previous studies showing a decaying cleaning effect as the coating dries for longer periods [45].

3. Bacterial coating preparation

To test the bubble-cleaning effect with live organisms, we also prepare glass slides coated with *E. coli*. For better visualization and precise data analysis, we introduce the green fluorescent protein (GFP) gene into *E. coli* (MM294 strain, Carolina Biological Supply Co.) with the heatshock plasmid transformation method. Using a disposable sterile pipette tip, we add 250 µl of 50 mM $CaCl_2$ solution to a sterile micro-tube. Then we use a sterile inoculation loop to transfer 5 *E. coli* colonies from the source media to the tube, and immerse the loop tip into the $CaCl_2$ solution and vigorously span the loop to disperse the entire mass into the $CaCl_2$ solution. The tube is then placed in an ice bath. Next, we transfer 10 µl of 0.01 µg/µl pGREEN (4528 bp) directly into the tube using a sterile pipette tip, and gently mix the solution. The tube is incubated in an ice bath for 10 min. After that, we take the tube to the 42°C water bath, and hold the tube under water for 45 s to give the bacteria colony a heat shock, and immediately return the tube on ice. After 2 min, we add 250 µl of recovery Luria broth (LB) to the tube. The resuspension is gently mixed, and incubated at room temperature for 10 min. We label 1 LB agar plate and 1 LB/Ampicillin+GFP agar plate. The Ampicillin plate is critical for selecting the GFP transformed bacteria colonies, and is made with 100 µl of 10 mg/ml Ampicillin solution and 20 ml agar media. Using a sterile P20 pipette tip, we transfer 50 µl of bacteria resuspension from the tube to each plate and spread the bacteria. The plates are rested for 10 min at room temperature, then sealed and incubated at 37ºC upside down. After 24 h of incubation, the GFP transformed colonies start to appear on the LB/Ampicillin+GFP plate. Using a sterile inoculation loop, we transfer the GFP transformed colonies to the LB broth and make a GFP *E. coli* resuspension. Next, in an aseptic experimental environment, we juxtapose four identical sterile glass slides inside a sterile Petri dish (140 mm diameter). We then add 33 ml of liquid LB agar media into the Petri dish to fully submerge the glass slides with agar media. We then let the agar cool down and solidify. The resulting thickness of the agar on each slide is controlled at 1 mm. We use a sterile pipette tip to transfer 25 µl of living *E. coli* resuspension to the middle of the agar plate. We then apply sterile glass beads on the plate to evenly distribute the bacteria. For further bacteria layer growth, the Petri dish is sealed with parafilm, and is rested for 10 min at room temperature to let the agar plate absorb the bacteria resuspension. Finally, the Petri dish is incubated at 37ºC for 72 h. After incubation, we gently cut the slides with the bacteria-agar layer on the top to use for the bubble cleaning experiments.

B. Bubble cleaning experiment

A 20 L tank is first filled with room temperature deionized water. Within it, a 3D printed slide-carrying tower holds coated slides at an angle, θ, with regards to the bottom of the tank as shown in Fig. 1(a). At the base of this slide carrier, a 25-gauge syringe needle is placed 5 mm from the slide edge at a constant height of 11 cm from the surface. A 3D printed needle holder connects the
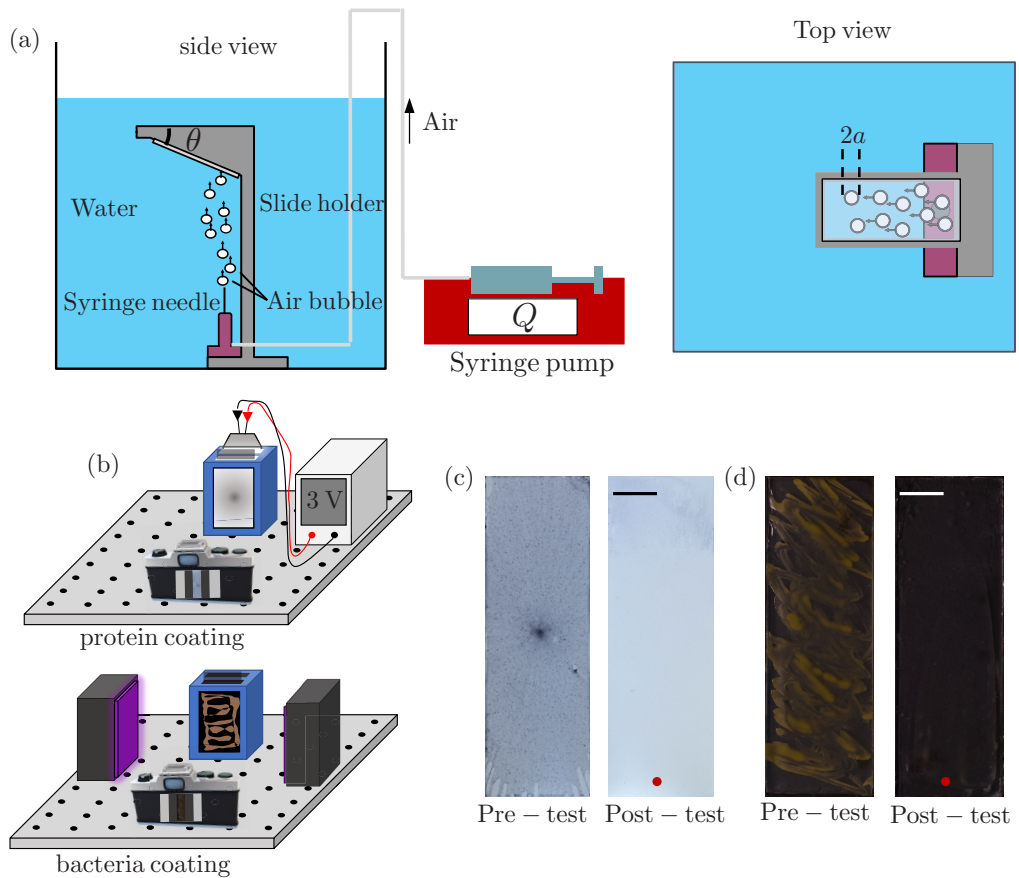
FIG. 1. (a) Side-view and top-view schematics of the experiments. (b) Schematics of the slide imaging setup. (c) Pretest and posttest images of a protein-coated slide for $\theta = 20^\circ$ and 6 min of bubble testing. (d) Pretest and posttest images of a biofilm coated slide for $\theta = 20^\circ$ and 6 min of testing. The red dots in the posttest images show the location of the bubble releaser.

syringe needle to an external syringe pump. Figure 1(a) shows the schematics for the side view and top view of the experiments.

Slides coated with proteins are imaged before and after each cleaning test utilizing a 3D printed LED slide stand fixed to an optical breadboard as illustrated in Fig. 1(b). The LED is maintained at 3V using a DC power supplier. The LED is replaced with a uniform black-painted background illuminated by a set of UV lights for the bacteria-coated slides. A digital camera (Nikon 7500) is fixed to the board 1.5 ft away from the slide with a 105 mm macro lens. The system is utilized in a dark room. Slide images from before and after the tests are then analyzed by performing image processing. We note that all the posttest images were taken after 1 h of drying in room temperature. Figures 1(c) and 1(d) show sample pretest and posttest images with protein coating and bacteria coating, respectively. We note that for protein coatings, there is always a darker spot appearing in the center of the slide indicative of a thicker coating layer, while some areas near the edges are thinner [see Fig. 1(c)]. However, since all slides are coated with the same method and include these features, the effect of such spots on the average cleaning results is negligible. On the contrary, surfaces coated with bacteria indicate more variations in the thickness of the biofilm, as shown in the pretest image of Fig. 1(d). To characterize the efficacy of bubble cleaning, the intensity matrix of the pretest, posttest, and clean-slide images are converted to grayscale matrices of I_1, I_2, and I_0,
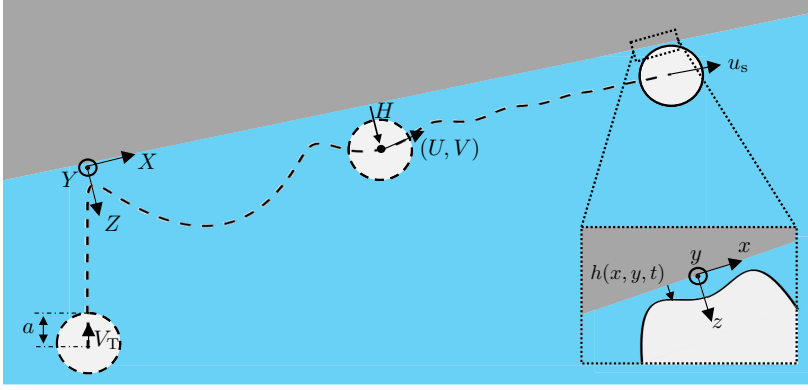
FIG. 2. Schematics of a bubble impacting a tilted surface from the bouncing to the sliding regime.

respectively. Hence, we define the total cleaning efficacy as $\lambda^t = (I_1 - I_2)/(I_1 - I_0)$. Therefore, as λ^t approaches 1, all coated contaminants are removed from the surface. To isolate the role of bubbles in cleaning, we run a series of control experiments with the same θ and cleaning time, T for each case where no bubbles are injected. We define the cleaning efficacy of the control experiments without bubbles in a similar way and denote it by λ^c. Then, we define the efficacy of cleaning bubbles as $\lambda = \lambda^t - \lambda^c$. It is noteworthy that λ^c for all cases is quite small compared to λ^t and does not change the trend between λ^t and λ significantly.

C. Numerical methods

To gain a more fundamental understanding of λ, we implement a numerical model that includes all forces that contribute to the dynamics of a bubble impacting a tilted surface: the buoyancy force, the drag force, the lift force, the added mass force, and the thin film force. We expect the liquid film thickness to be on the order of micrometers and a stable liquid film force remains significant as the bubble moves near the tilted wall [11,26]. This model has previously been discussed and studied for a similar condition where the bubble impacts and slides over a tilted wall [11]. Hence, we only summarize the main features of the model herein and refer to Ref. [11] for further details. We note that in this study we focus on features of bubble dynamics that are different from previous work [11] to rationalize our current experimental results.

Figure 2 shows the schematic of a bubble impacting a tilted surface to introduce the notations used in our model. Both XYZ and xyz coordinates denote the axial direction, the transverse direction, and the direction normal to the surface, respectively. The XYZ origin is located on the first impact point, while the xyz origin is the bubble's centroid projected onto the surface which moves with the bubble. The bubble's centroid distance normal to the surface is denoted by H while it moves with velocities U, and V, along X and Z, respectively. In addition, the thin film thickness and the thin film pressure are denoted by $h(x, y, t)$ and $P(x, y, t)$, respectively. Hence, the force balance in X and Z yields as [11]

$$\rho\Omega\left[C_m^{||}\frac{dU}{dt} - \frac{dC_{m||}^{||}}{dH}VU\right] = \rho g\Omega\sin(\theta) - \frac{\pi}{4}C_D^{||}\text{Re}\mu Ua - \iint_A P_f\frac{dh}{dx}dxdy + C_L\rho\Omega V\omega_y, \quad (1)$$

and

$$\rho\Omega\left[C_m^{\perp}\frac{dV}{dt} + \frac{1}{2}\left(\frac{dC_m^{||}}{dH}U^2 - \frac{dC_m^{\perp}}{dH}V^2\right)\right]$$

$$= \rho g\Omega\cos(\theta) - \frac{\pi}{4}C_D^{\perp}\text{Re}\mu Va - \iint_A P_f dxdy - C_L\rho\Omega U\omega_y, \quad (2)$$
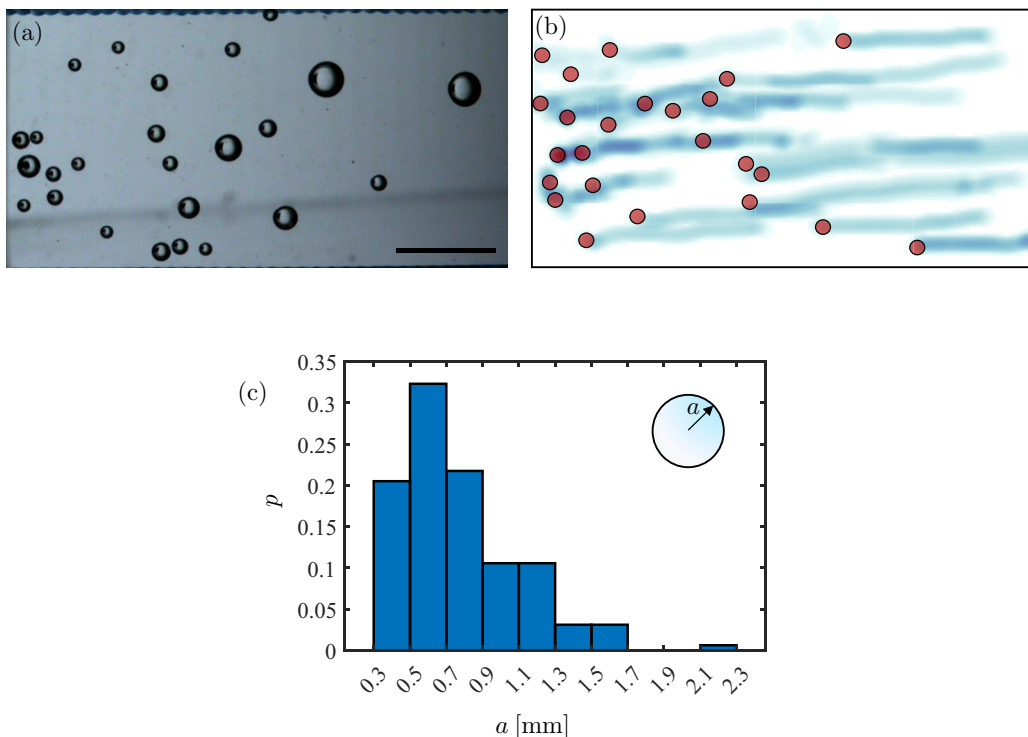
FIG. 3. (a) Snapshot of bubbles moving along a clean surface with $\theta = 10^{\circ}$. (b) Trajectory of air bubbles for 0.4 s presented using an arbitrary color with a Gaussian blurring method at bubble centers. The Gaussian distribution has a root mean square width equal to a bubble radius. The red circles highlight the collision point of bubbles on the surface. (c) Histogram of bubbles radius, a, for five different tests and approximately 200 bubbles.

respectively. Here, ρ denotes the air density, Ω denotes the bubble volume, and μ denotes the dynamic viscosity of water. $\mathrm{Re} = 2\rho_{\mathrm{w}}V_{\mathrm{T}}a/\mu$ is the Reynolds number with ρ_{w} denoting the water density and V_{T} denoting the bubble's terminal rising velocity. C_{m}, C_{D}, and C_{L} denote the coefficients of added mass, drag, and lift, respectively. The components of these coefficients along X and Z are denoted with superscripts || and $\perp$, respectively. We take $C_{\mathrm{m}}^{\perp} = C_{\mathrm{m}}^{||} = 0.5$, and $C_{\mathrm{L}} = 0.5$, both reasonably assumed constants [11]. In addition, we use $C_{\mathrm{D}}^{||} = (48/\mathrm{Re})[-1 + 0.5(1/2b)^3]^{-2}$ and $C_{\mathrm{D}}^{\perp} = (48/\mathrm{Re})[-1 + (1/2b)^3]^{-2}$, where $b = (H + a)/a$ [56,57]. The terms on the left-hand side of Eqs. (1) and (2) refer to the inertia terms including the added mass force, while the right-hand side terms correspond to the buoyancy force, the drag force, the thin film force, and the lift force, respectively. It is noteworthy that the lift force is only noticeable between the first two collisions as vorticity, ω_y is induced by the rising wake flow circulating around the bouncing bubble [44]. More details about the expressions used for each coefficient and how the thin film force is calculated can be found in Ref. [11].

The domain is divided into 105×105 nodes. The equations are discretized using a finite difference method and are solved using a MATLAB ode15s solver. We make sure that all forces are continuously computed over the entire time without any discontinuity. Taking into account the size distribution of the bubbles presented in Fig. 3(c), we incorporate $a = 0.6$ mm into our model, as it represents the most frequent bubble size in the experiments. It is assumed that the bubble is at $H = 3$ mm from the surface at $t = 0$ while rising with a measured terminal rising velocity, $V_{\mathrm{T}} \approx 32$ cm/s. Since, in the experiments, the axial distance between the projection of the bubble
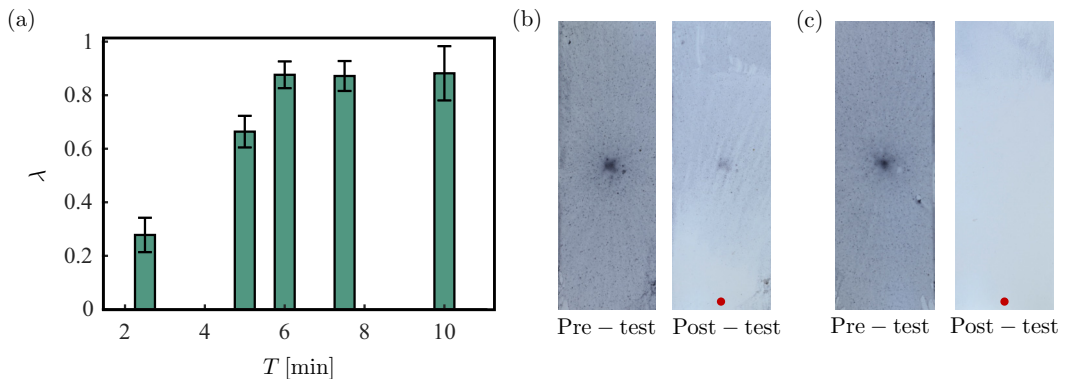
FIG. 4. (a) The cleaning efficacy, λ, for varying test time, T, at $\theta = 20^\circ$. (b) Pretest and posttest images of a surface coated with protein for $T = 5$ min, and $\theta = 20^\circ$. The scale bar shows 1 cm. (c) Pretest and posttest images of a surface coated with protein for $T = 6$ min, and $\theta = 20^\circ$. The red dots in posttest images show the location of the bubble releaser. The scale bar shows 1 cm.

releaser on the surface and the edge of the surface is 6 cm, we assume that bubbles travel an average of 6 cm along X in the model. Hence, we model the bubble motion from $t = 0$ until it reaches $X = 6$ cm. We note that $X = 6$ cm is well beyond the threshold of transitioning from bouncing to sliding regime.

III. RESULTS

We first extract the size distribution for bubbles generated from the 25-gauge needle used at a constant flow rate of $Q = 10$ ml/min in all experiments. Figure 3(a) shows a sample snapshot of bubbles moving along a surface with $\theta = 10^\circ$ from the top view. Figure 3(b) shows surface areas covered by air bubbles over a duration of 0.4 s indicated by using a Gaussian blur at the centers of the bubbles with a root mean square width equal to their radii for the purpose of demonstration. As shown in Fig. 3(b), bubbles adequately cover the slide along the transverse direction. The darker colors near the left end indicate the slower tangential motion of the bubbles along the surface near their impact point. Figure 3(c) shows the probability histogram of the extracted bubble radius, a, for five different trials over 200 bubbles. Here, $a = 0.6$ mm is the most frequent average bubble size as the bubble radius in the model.

We first run a series of protein tests with different cleaning times, T. Figures 4(b) and 4(c) show the pretest and posttest images at $\theta = 20^\circ$ with two different times: $T = 5$ min and $T = 6$ min, respectively. Figure 4(a) shows λ for $T = 2.5, 5, 6, 7.5$, and 10 min with $\theta = 20^\circ$. As indicated in Fig. 4(a), λ increases with T until it plateaus out after $T = 6$ min. Therefore, we choose $T = 6$ min as the reference test time on surfaces coated with proteins with different θ. Next, we perform the cleaning experiments at five different angles, $\theta = 5^\circ, 10^\circ, 20^\circ, 30^\circ$, and 40° for 6 min. As shown in Fig. 5(a), the cleaning efficacy, λ, first increases with angle up to $\theta > 20^\circ$, then decreases rapidly. Two representative cases ($\theta = 10^\circ$ and $\theta = 20^\circ$) are shown in Figs. 5(b) and 5(c), respectively.

In addition, we conduct cleaning experiments with surfaces coated with bacterial biofilm following the procedure described in Sec. II A 3. We note that the biofilm tests are all conducted for 2 min to avoid any delamination of the film and catch up with the fast removal time. Also, we notice that λ does not increase noticeably for bacteria tests beyond 2 min of the experiment. Figure 6(a) shows that the maximum λ occurs at $\theta = 20^\circ$ similar to the protein tests. Figures 6(b) and 6(c) show the pretest and posttest images from two cases corresponding to $\theta = 10^\circ$ and $\theta = 20^\circ$, respectively.

Next, let us discuss the results obtained from the numerical model that was described in Sec. II C. The average shear force, $\overline{F}_\mathrm{s}$, exerted by the bubble on the surface is the key parameter relevant to
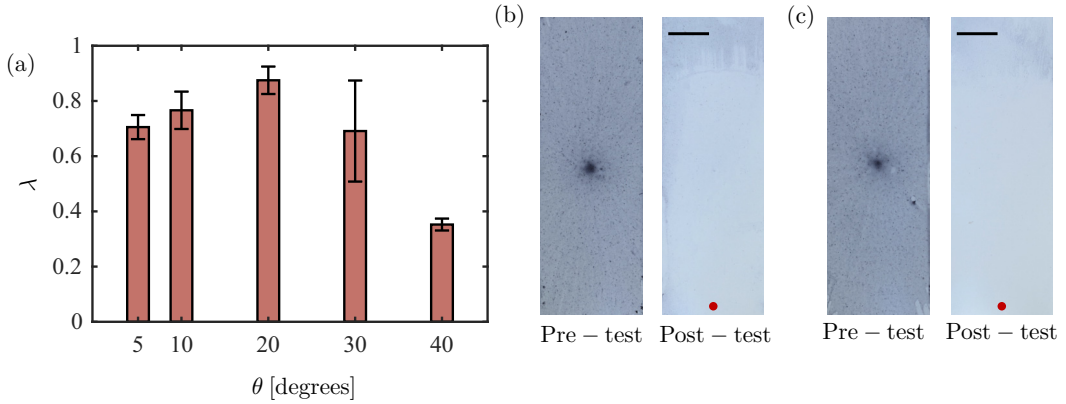
FIG. 5. (a) The efficacy of cleaning, λ, on surfaces coated with proteins for varying surface angles, θ, with $T = 6$ min. (b) Pretest and posttest images for $\theta = 10°$, and $T = 6$ min. The scale bar shows 1 cm. (c) Pretest and posttest images for $\theta = 20°$, and $T = 6$ min. The red dots in the posttest images show the location of the bubble releaser. The scale bar shows 1 cm.

cleaning experiments. To characterize $\overline{F}_s$, we need to discuss two primary factors that affect the shear force of a bubble: the steady film thickness and the steady sliding speed. Figure 7 shows the 3D bubble shape during the steady sliding regime for $a = 0.6$ mm, and $\theta = 20°$. During the steady sliding regime, the bubble shape and the thin film profile do not change noticeably. Figure 7 inset shows the zoom-in view of the 3D bubble shape close to the surface where a dimple forms as previously reported [11,58,59].

To gain better insight into the shear force on the surface, we explore the 2D bubble profile in the x-z plane for $y = 0$ μm, 100 μm, and 200 μm. Figure 8 indicates the bubble profile for $\theta = 10°$, $\theta = 20°$, and $\theta = 30°$ along different x-z planes. The solid line shows the bubble shape along the central axis, while the dashed line and the dotted dashed line show the profile at $y = 100$ μm and $y = 200$ μm off from the centerline, respectively. The inset plot shows a zoom-in profile near the centerline. Figure 8 shows that the thickness of the film increases with increasing θ. In addition, the dashed lines in Fig. 8 indicate that the dimple size is less than 100 μm from the center along
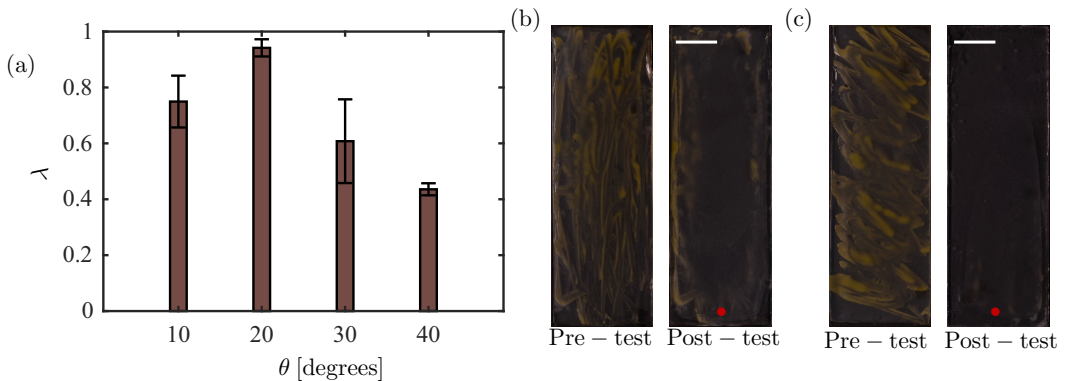

FIG. 6. (a) The cleaning efficacy, λ, on surfaces coated with bacteria for varying surface angles, θ, with $T = 6$ min. (b) Pretest and posttest images for $\theta = 10°$, and $T = 6$ min. The scale bar shows 1 cm. (c) Pretest and posttest images for $\theta = 20°$, and $T = 6$ min. The red dots in posttest images show the syringe needle projection on the surface. The scale bar shows 1 cm.
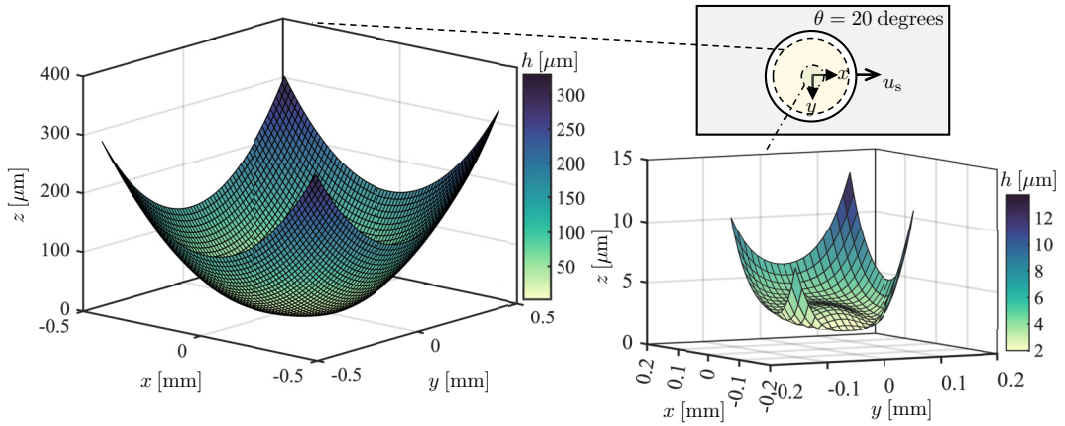
FIG. 7. Bubble profile for $a = 0.6$ mm and $\theta = 20°$ during the steady-state sliding. The inset shows the zoom-in view of the dimple formed on the bubble, near the solid surface.

y. Fig. 8 also reveals a lower minimum height on the receding side of the dimple compared to the advancing side. The film thickness on the receding side is of great importance, as the shear force on the surface is mainly composed of the cumulative shear force terms from this thin region. Figure 9 shows the bubble 2D profile in the y-z plane at $x = 0\,\mu$m, $100\,\mu$m, and $200\,\mu$m with the titled angle of $\theta = 10°$, $20°$, and $30°$. The bubble profile is symmetric about the plane of $y = 0$ as shown in Fig. 9. Additionally, Fig. 9 shows that the dimple width decreases with increasing θ.

Figure 10 shows the steady sliding velocity, u_s, with different angles. As indicated in Fig. 10, u_s computed from the model is in good agreement with the experiments. The experimental data presented in Fig. 10 are collected in a separate series of experiments in which single air bubbles with $a = 0.6$ mm and a standard deviation of 0.03 mm are recorded while injected individually. To discuss our results, we consider Eqs. (1) and (2) during the steady sliding phase where the inertia terms on the left-hand side of both equations tend to zero as $V = 0$, $d/dt = d/dH = 0$. We also note that the lift force on the right-hand side of Eqs. (1) and (2) tend to zero as $\omega_y \approx 0$
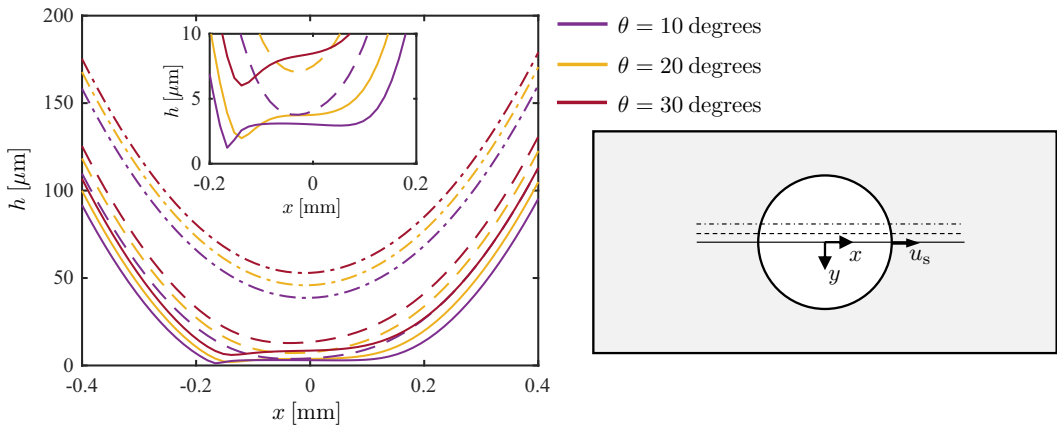

FIG. 8. The bubble profile during the steady-state sliding in x-z planes at $y = 0\,\mu$m (solid line), $y = \pm 100\,\mu$m (dashed line), and $y = \pm 200\,\mu$m (dotted dashed line) with $a = 0.6$ mm for $\theta = 10°$ (violet), $\theta = 20°$ (yellow), and $\theta = 30°$ (red). The inset shows the zoom in view of the profile near the centerline.

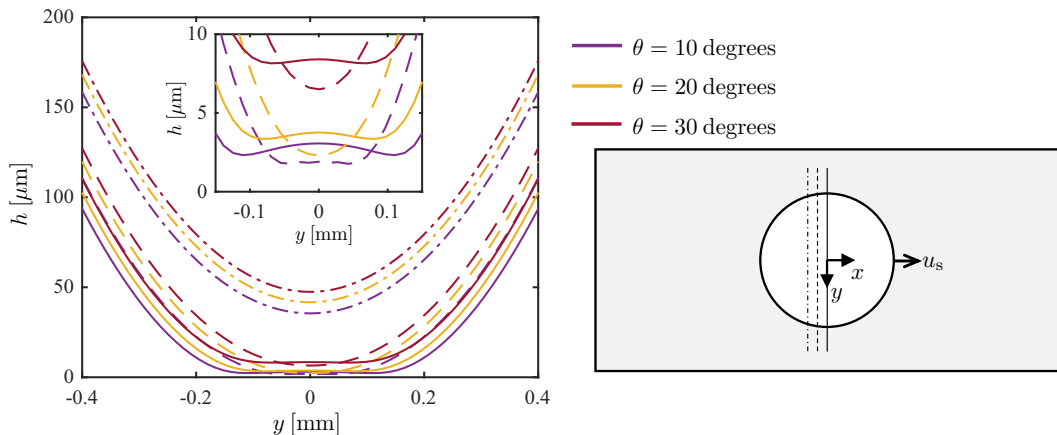FIG. 9. The bubble profile during the steady-state sliding in y-z planes at $x = 0$ µm (solid line), $x = \pm 100$ µm (dashed line), and $x = \pm 200$ µm (dotted dashed line) with $a = 0.6$ mm for $\theta = 10°$ (violet), $\theta = 20°$ (yellow), and $\theta = 30°$ (red). The inset shows the zoom-in view of the profile near the centerline.

after the bouncing phase. Considering a sphere of radius a sliding along a flat surface with a minimum gap thickness, h_0, in a fluid with dynamic viscosity, μ, the thin film force scales as $\mu u_s a^2 / h_0$ along Z and $-\mu u_s a \ln(h_0/a)$ along X [60]. The logarithmic dependence is weaker than the inverse dependence. Hence, for simplicity, we consider up to the order of $\mathcal{O}(a/h_0)$ and ignore the logarithmic dependence. Note that the drag term in Eqs. (1) and (2) linearly depend on the velocity and bubble size as long as $(H + a)/a$ is constant. Then, both drag force and thin film force scale as $\mu u_s a$ along X which must balance with the buoyant force scaling as $\rho g a^3 \sin\theta$. Hence, $u_s \propto (\rho g a^2 / \mu) \sin\theta$. Figure 10 shows that $u_s = 0.25 \sin\theta$ [m/s] gives a good match with experiments.

However, the two leading order terms in force balance along Z are buoyancy and thin film force which yield $\rho g a^3 \cos\theta \propto \mu u_s a^2 / h_0$, hence $h_0 \propto a \tan\theta$. Furthermore, as shown in Fig. 11(a), h_0 scales with $c_1 + c_2 \tan 2\theta$ rather than $\tan\theta$ by itself in comparison with the numerical results. This is
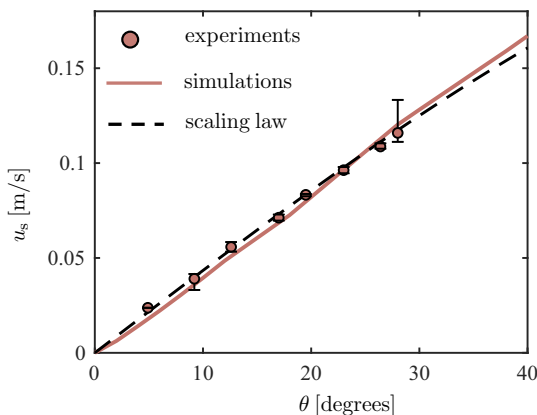

FIG. 10. Comparison of the steady-state sliding velocity, u_s for varying θ between the experiments (symbols), the model (solid line), and the scaling laws (dashed line). The dashed line shows $u_s = 0.25 \sin\theta$. The error bars represent three trials.
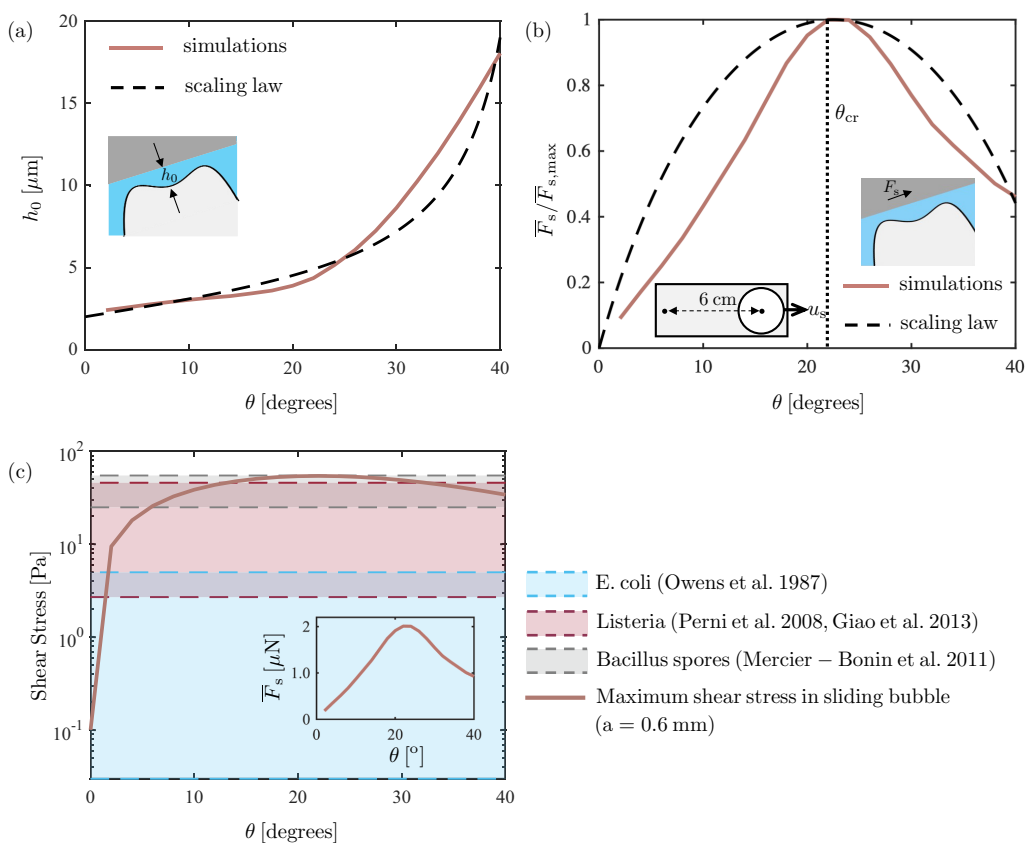
FIG. 11. (a) Numerical model (solid line) and scaling law (dashed line) results for the steady film thickness in the center of the bubble, h_0, at varying θ. (b) Model results (solid line) and scaling law (dashed line) for the average shear force, $\overline{F}_s$, normalized by maximum $\overline{F}_s$ at varying θ. The dashed line shows $\overline{F}_s = 7 \times 10^{-6} \sin\theta \cos(2\theta)$. (c) The maximum shear stress in the steady sliding phase for $a = 0.6$ mm and varying θ. The shaded areas show limits reported for removing *E. coli* [51], *Listeria* [54,61], and *Bacillus* spores [62]. The inset shows $\overline{F}_s$ magnitude vs θ.

presumably due to the complex hydrodynamic coupling between different directional forces, which is not considered in this simple scaling argument.

Next, we compute the mean shear force on the surface along X as $\overline{F}_s = \frac{1}{L}\int_0^L F_s\, dX$ where F_s denotes the temporal shear force on the surface, and $L = 6$ cm denotes the total length traveled by the bubble parallel to the surface. We note that $\overline{F}_s$ beyond 6 cm does not change significantly. Hence, the resulting average value is close to the steady-state value. However, decreasing the integration domain to a length scale comparable to the length of the bouncing regime may lead to a different result which is out of the scope of the current study. As shown in Fig. 11(b), our model gives the maximum $\overline{F}_s$ at about $\theta \simeq 23°$ close to experimental findings in Figs. 5 and 6. Following the simple scaling discussed above, the shear drag scales as $\overline{F}_s \propto \mu u_s/h_0 \propto \rho g a \sin\theta/(c_1 + c_2 \tan 2\theta)$. We also show the maximum shear stress over the surface during the steady sliding phase in Fig. 11(c) and compare it with reported critical shear stress required for removing different types of bacteria [51,54,61,62]. For instance, while the maximum shear stress for $\theta > 2°$ can remove *E. coli*, removing *Listeria* requires $15° < \theta < 30°$. Hence, by considering the adhesion and cohesion stresses in a biofilm or soil layer, certain angle range can be decided for designing cleaning strategies.
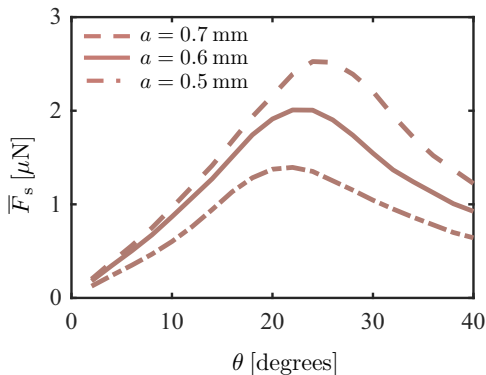
FIG. 12. $\overline{F}_s$ vs θ for different bubble sizes, $a = 0.5$, 0.6, and 0.7 mm.

Finally, we repeat the simulations for $a = 0.5$ mm and $a = 0.7$ mm using the rising terminal velocity of bubbles measured from experiments. As shown in Fig. 12, the maximum shear force increases with the bubble size while the optimum angle is slightly shifted from 20° to 25°. It is noteworthy that our model is not valid beyond $a = 0.7$ mm as bubbles no longer retain a spherical shape during sliding and their sliding speed and film profile deviate from the current model. Hence, in the working limit of our model, we can conclude that best cleaning results can be achieved for $a = 0.6$–0.7 mm in a range of $\theta = 20°$ and 25°.

IV. DISCUSSIONS

We examined the cleaning effect of millimetric bubbles at different inclination angles of the substrate coated with either proteins or bacterial biofilm. Our results indicated that both coatings produce similar cleaning results, where $\theta \simeq 22°$ gives the highest cleaning parameter, λ. This consistent result with both protein coating and bacterial coating suggests that surface wettability is not a key factor in cleaning, but that the angle of inclination is. We also computationally investigated the bubble collision at different surface angles from the first impact moment until the bubble reaches the edge of the surface in a steady sliding regime. Our numerical model indicated that while the steady sliding speed increases with the inclination angle, the characteristic film thickness between the bubble and the surface also increases. Since the sliding speed and the film thickness have counter effects on the shear stress applied to the surface, their interaction yields the maxima in shear force versus surface angle.

The current study investigates the role of surface geometry (i.e., inclination angle) in the use of air bubbles as a sustainable method to effectively sanitize surfaces contaminated with active or passive coatings. Our experiments showed a maximum cleaning effect in tilted surfaces, and our numerical model revealed that the interplay between the sliding speed of the bubble and the film thickness set the maximum cleaning angle for a single bubble size. We also showed that the maximum shear force occurs at a similar range of θ for slight variations in bubble size. While our model explained the mechanism that set the maximum cleaning angle, we note that the current model considered the bubble collision and sliding dynamics in a simplified case of "contaminant-free" medium where a shear-free boundary condition on bubble surface is valid throughout. However, in our cleaning experiments and real cleaning applications we expect the bubble to transition from a mobile surface to an immobile surface with zero tangential velocity after holding contaminants on the bubble surface. The immobile condition on the bubble surface reduces the rising velocity [26], which is expected to reduce the shear force applied to the surface. The role of tilting angle on the steady sliding speed and steady film thickness for an immobile bubble is not trivial and needs to be evaluated by further future studies. This method can be advantageous in cleaning surfaces of

soft materials such as fruits and vegetables, where conventional methods damage the soft tissues of the produce. In addition, our findings on the optimal cleaning angle can be leveraged to design bubble-cleaning machinery applicable to biomedical devices. Further studies are required to fully characterize the role of bubble size on the most effective angle to account for polydisperse bubble injection. In addition, studying bubble dynamics on curved surfaces is a relevant topic that will be addressed in the future study.

[1] S. B. G. O'Brien and B. H. A. A Van Den Brule, A mathematical model for the cleansing of silicon substrates by fluid immersion, J. Colloid Interface Sci. **144**, 210 (1991).

[2] C. G. Suárez, J. Noordmans, H. C. van der Mei, and H. J. Busscher, Removal of colloidal particles from quartz collector surfaces as stimulated by the passage of liquid–air interfaces, Langmuir **15**, 5123 (1999).

[3] S. Khodaparast, M. K. Kim, J. E. Silpe, and H. A. Stone, Bubble-driven detachment of bacteria from confined microgeometries, Environ. Sci. Technol. **51**, 1340 (2017).

[4] P. R. Gogate and A. B. Pandit, A review of imperative technologies for wastewater treatment I: Oxidation technologies at ambient conditions, Adv. Environ. Res. **8**, 501 (2004).

[5] Y. J. Chan, M. F. Chong, C. L. Law, and D. G. Hassell, A review on anaerobic–aerobic treatment of industrial and municipal wastewater, Chem. Eng. J. **155**, 1 (2009).

[6] T. Temesgen, T. T. Bui, M. Han, T. Kim, and H. Park, Micro and nanobubble technologies as a new horizon for water-treatment techniques: A review, Adv. Colloid Interface Sci. **246**, 40 (2017).

[7] M. Menesses, J. Belden, N. Dickenson, and J. Bird, Measuring a critical stress for continuous prevention of marine biofouling accumulation with aeration, Biofouling **33**, 703 (2017).

[8] G. A. Hopkins, F. Gilbertson, O. Floerl, P. Casanovas, M. Pine, and P. Cahill, Continuous bubble streams for controlling marine biofouling on static artificial structures. PeerJ **9**, e11323 (2021).

[9] C. D. Ohl, M. Arora, R. Dijkink, V. Janve, and D. Lohse, Surface cleaning from laser-induced cavitation bubbles, Appl. Phys. Lett. **89**, 074102 (2006).

[10] J. J. Lee, J. D. Eifert, S. Jung, and L. K. Strawn, Cavitation bubbles remove and inactivate *Listeria* and *Salmonella* on the surface of fresh Roma tomatoes and cantaloupes, Front. Sustain. Food Syst. **2**, 61 (2018).

[11] E. Esmaili, P. Shukla, J. D. Eifert, and S. Jung, Bubble impact on a tilted wall: Removing bacteria using bubbles, Phys. Rev. Fluids **4**, 043603 (2019).

[12] C. D. Ohl, M. Arora, R. Ikink, N. De Jong, M. Versluis, M. Delius, and D. Lohse, Sonoporation from jetting cavitation bubbles, Biophys. J. **91**, 4285 (2006).

[13] B. Verhaagen and D. F. Rivas, Measuring cavitation and its cleaning effect, Ultrason. Sonochem. **29**, 619 (2016).

[14] F. Reuter and R. Mettin, Mechanisms of single bubble cleaning, Ultrason. Sonochem. **29**, 550 (2016).

[15] G. L. Chahine, A. Kapahi, J. K. Choi, and C. T. Hsiao, Modeling of surface cleaning by cavitation bubble dynamics and collapse, Ultrason. Sonochem. **29**, 528 (2016).

[16] A. T. Kriegel and W. A. Ducker, Removal of bacteria from solids by bubbles: Effect of solid wettability, interaction geometry, and liquid–vapor interface velocity, Langmuir **35**, 12817 (2019).

[17] S. Jung and J. Eifert, Cleaning fruits using micro-bubbles (2016), http://www.foodonline.com/doc/cleaning-fruits-using-micro-bubbles-0001

[18] E. Scallan, R. M. Hoekstra, F. J. Angulo, R. V. Tauxe, M. Widdowson, S. L. Roy, J. L. Jones, and P. M. Griffin, Foodborne illness acquired in the United States—Major pathogens, Emerg. Infect. Dis. **17**, 7 (2011).

[19] E. Scallan, P. M. Griffin, F. J. Angulo, R. V. Tauxe, and R. M. Hoekstra, Foodborne illness acquired in the United States—Unspecified agents, Emerg. Infect. Dis. **17**, 16 (2011).

[20] J. G. Morris, Jr., How safe is our food? Emerg. Infect. Dis. **17**, 126 (2011).

[21] R. Clift, J. R. Grace, and M. E. Weber, *Bubbles, Drops, and Particles* (Courier Corporation, North Chelmsford, Chelmsford, MA, 2005).

[22] P. C. Duineveld, The rise velocity and shape of bubbles in pure water at high Reynolds number, J. Fluid Mech. **292**, 325 (1995).

[23] L. Amaya-Bower and T. Lee, Single bubble rising dynamics for moderate Reynolds number using lattice Boltzmann method, Comput. Fluids **39**, 1191 (2010).

[24] F. Peters and C. Els, An experimental study on slow and fast bubbles in tap water, Chem. Eng. Sci. **82**, 194 (2012).

[25] M. Wu and M. Gharib, Experimental studies on the shape and path of small air bubbles rising in clean water, Phys. Fluids **14**, L49 (2002).

[26] R. Manica, E. Klaseboer, and D. Y. C. Chan, Force balance model for bubble rise, impact, and bounce from solid surfaces, Langmuir **31**, 6763 (2015).

[27] J. Zawala, "Immortal" liquid film formed by colliding bubble at oscillating solid substrates, Phys. Fluids **28**, 057103 (2016).

[28] J. Zawala, D. Kosior, T. Dabros, and K. Malysa, Influence of bubble surface fluidity on collision kinetics and attachment to hydrophobic solids, Colloids Surf. A **505**, 47 (2016).

[29] M. Krasowska and K. Malysa, Kinetics of bubble collision and attachment to hydrophobic solids: I. Effect of surface roughness, Int. J. Miner. Process. **81**, 205 (2007).

[30] R. Zenit and D. Legendre, The coefficient of restitution for air bubbles colliding against solid walls in viscous liquids, Phys. Fluids **21**, 083306 (2009).

[31] E. Klaseboer, R. Manica, M. H. W. Hendrix, C. Ohl, and D. Y. C. Chan, A force balance model for the motion, impact, and bounce of bubbles, Phys. Fluids **26**, 092101 (2014).

[32] A. W. G. de Vries, A. Biesheuvel, and L. van Wijngaarden, Notes on the path and wake of a gas bubble rising in pure water, Int. J. Multiphase Flow **28**, 1823 (2002).

[33] F. Takemura and J. Magnaudet, The transverse force on clean and contaminated bubbles rising near a vertical wall at moderate Reynolds number, J. Fluid Mech. **495**, 235 (2003).

[34] M. F. Moctezuma, R. Lima-Ochoterena, and R. Zenit, Velocity fluctuations resulting from the interaction of a bubble with a vertical wall, Phys. Fluids **17**, 098106 (2005).

[35] B. Figueroa-Espinoza, R. Zenit, and D. Legendre, The effect of confinement on the motion of a single clean bubble, J. Fluid Mech. **616**, 419 (2008).

[36] T. Maxworthy, Bubble rise under an inclined plate, J. Fluid Mech. **229**, 659 (1991).

[37] H. Tsao and D. L. Koch, Observations of high Reynolds number bubbles interacting with a rigid wall, Phys. Fluids **9**, 44 (1997).

[38] A. Perron, L. I. Kiss, and S. Poncsák, An experimental investigation of the motion of single bubbles under a slightly inclined surface, Int. J. Multiphase Flow **32**, 606 (2006).

[39] B. Podvin, S. Khoja, F. Moraga, and D. Attinger, Model and experimental visualizations of the interaction of a bubble with an inclined wall, Chem. Eng. Sci. **63**, 1914 (2008).

[40] C. E. Norman and M. J. Miksis, Dynamics of a gas bubble rising in an inclined channel at finite Reynolds number, Phys. Fluids **17**, 022102 (2005).

[41] K. M. DeBisschop, M. J. Miksis, and D. M. Eckmann, Bubble rising in an inclined channel, Phys. Fluids **14**, 93 (2002).

[42] C. Barbosa, D. Legendre, and R. Zenit, Sliding motion of a bubble against an inclined wall from moderate to high bubble Reynolds number, Phys. Rev. Fluids **4**, 043602 (2019).

[43] A. Hooshanginejad, A. Baskota, and S. Jung, A backflipping motion of a bubble impacting tilted surfaces, in *APS Division of Fluid Dynamics Meeting Abstracts* (APS, College Park, MD, 2021), p. A21.004.

[44] A. Hooshanginejad, A. Baskota, and S. Jung, Backflipping motion of air bubbles colliding with a tilted wall, arXiv:2208.14486.

[45] A. Hooshanginejad, T. J. Sheppard, J. Manyalla, J. Jaicks, and S. Jung, Cleaning effect of bubbles impacting tilted walls under acoustic waves, in *Proceedings of the ASME 2022 Fluids Engineering Division*

Summer Meeting, Volume 2: Multiphase Flow (MFTC); Computational Fluid Dynamics (CFDTC); Micro and Nano Fluid Dynamics (MNFDTC) (ASME, Toronto, Ontario, 2022).

[46] C. E. Zobell, The effect of solid surfaces upon bacterial activity. J. Bacteriol. **46**, 39 (1943).

[47] K. C. Marshall, R. Stout, and R. Mitchell, Mechanism of the initial events in the sorption of marine bacteria to surfaces, Microbiology **68**, 337 (1971).

[48] K. C. Marshall and R. H. Cruickshank, Cell surface hydrophobicity and the orientation of certain bacteria at interfaces, Archiv. Mikrobiol. **91**, 29 (1973).

[49] H. H. Tuson and D. B. Weibel, Bacteria-surface interactions. Soft Matter **9**, 4368 (2013).

[50] N. P. Boks, W. Norde, H. C. van der Mei, and H. J. Busscher, Forces involved in bacterial adhesion to hydrophilic and hydrophobic surfaces, Microbiology **154**, 3122 (2008).

[51] N. F. Owens, D. Gingell, and P. R. Rutter, Inhibition of cell adhesion by a synthetic polymer adsorbed to glass shown under defined hydrodynamic stress, J. Cell Sci. **87**, 667 (1987).

[52] M. Mukumoto, T. Ohshima, M. Ozaki, H. Konishi, N. Maeda, and Y. Nakamura, Effect of microbubbled water on the removal of a biofilm attached to orthodontic appliances—An *in vitro* study, Dent. Mater. J. **31**, 821 (2012).

[53] J. E. Duddridge, C. A. Kent, and J. F. Laws, Effect of surface shear stress on the attachment of pseudomonas fluorescens to stainless steel under defined flow conditions, Biotechnol. Bioeng. **24**, 153 (1982).

[54] M. S. Gião and C. W. Keevil, Hydrodynamic shear stress to remove *Listeria monocytogenes* biofilms from stainless steel and polytetrafluoroethylene surfaces, J. Appl. Microbiol. **114**, 256 (2013).

[55] P. K. Sharma, M. J. Gibcus, H. C. Van Der Mei, and H. J. Busscher, Microbubble-induced detachment of coadhering oral bacteria from salivary pellicles, Eur. J. Oral Sci. **113**, 326 (2005).

[56] C. W. M. Van der Geld, On the motion of a spherical bubble deforming near a plane wall, J. Eng. Math. **42**, 91 (2002).

[57] C. W. M. Van der Geld, H. Van Wingaarden, and B. A. Brand, Experiments on the effect of acceleration on the drag of tapwater bubbles, Exp. Fluids **31**, 708 (2001).

[58] D. Platikanov, Experimental investigation on the "dimpling" of thin liquid films, J. Phys. Chem. **68**, 3619 (1964).

[59] L. Pan, S. Jung, and R. Yoon, Effect of hydrophobicity on the stability of the wetting films of water formed on gold surfaces, J. Colloid Interface Sci. **361**, 321 (2011).

[60] A. Hooshanginejad, S. Jung, E. Longmire, and S. Lee, Gravity-induced double encapsulation of liquids using granular rafts, Phys. Rev. Fluids **7**, 064003 (2022).

[61] S. Perni, E. S Read, and G. Shama, Detachment of *Listeria innocua* and *Pantoea agglomerans* from cylinders of agar and potato tissue under conditions of Couette flow, J. Food Eng. **89**, 355 (2008).

[62] M. Mercier-Bonin, A. Dehouche, J. Morchain, and P. Schmitz, Orientation and detachment dynamics of bacillus spores from stainless steel under controlled shear flow: Modelling of the adhesion force, Int. J. Food Microbiol. **146**, 182 (2011).